A comparison of computational models for wrinkling of pressurized shell-core systems

Tomo Veldin [a], Marko Lavrenčič [b], Boštjan Brank [b], Miha Brojan [a],*

[a] *University of Ljubljana, Faculty of Mechanical Engineering, Laboratory for Nonlinear Mechanics, Askerceva c. 6, SI-1000 Ljubljana, Slovenia*
[b] *University of Ljubljana, Faculty of Civil and Geodetic Engineering, Jamova c. 2, SI-1000 Ljubljana, Slovenia*

ARTICLE INFO

ABSTRACT

Four nonlinear computational models for the surface wrinkling of curved shell-core systems under external pressure are presented. Three of the considered finite element models neglect the displacements tangential to the shell surface. Two of the models are static formulations and the other two are derived in the dynamic framework. For the latter, the energy-decaying time-stepping algorithm is applied, which is suitable for numerically stiff problems, such as shell-core systems, characterized by stiff membrane and soft wrinkling deformation modes. In all cases the core is modeled by elastic springs. As a comparative problem we choose the surface wrinkling of pressurized shell-core spheres. In particular, five systems with different material and geometric properties are computed, which have different wrinkle patterns. A good agreement is found between the results of the models as well as with the relevant references, which provide numerical and experimental results. However, it has been observed that our reduced-order models are blind to the prediction of the secondary transformation – from the dimple-like pattern to the labyrinthine pattern. Another conclusion is that a non-tailored (i.e. standard) shell finite element on an elastic foundation combined with the energy-decaying scheme, provides excellent predictions of the surface wrinkle patterns.

1. Introduction

Instabilities of thin films on soft substrates exhibit a rich variety of deformation modes and associated periodic buckling patterns. Especially the patterns developed during surface wrinkling are interesting in engineering, as they serve as a basis for many advanced applications (e.g. active control of wetting to achieve hydrophobicity/hydrophilicity [1], smart adhesion [2], flexible electronics [3], thin film metrology [4], tunable aerodynamic drag [5], etc.), which would otherwise be much more difficult (or impossible) to implement. Deformation modes such as wrinkling, creasing, folding, etc. are also of interest in the biology of tissues, especially in organogenesis, since they can be used for the preliminary (mechanistic) description of morphogenesis during the growth of e.g. intestine [6], brain [7] and lung [8], growth of bacterial biofilms [9,10], etc. More about wrinkling patterns and mechanisms can be found e.g. in a recent review paper by Tan et al. [11].

For all these examples, a sound computational model, capable of accurately predicting the deformation mechanisms is essential. At first glance, the task of creating such a model may seem very simple. For example, wrinkling on spheres (which is also addressed in this paper) can be defined by only three basic components: We need (*i*) a thin spherical shell which is adhered to (*ii*) a soft substrate and

(*iii*) an external hydrostatic pressure load. Note that the key in this definition is the mismatch between the Young moduli of the shell and the substrate (and the external pressure), but analogous problems can be defined by considering the temperature loading and the mismatch of the linear thermal expansion coefficients [12], the faster growth of the shell [13], etc. However, it turns out that this shell/substrate structure is remarkably difficult to solve because it has a very complex response in terms of strong geometric nonlinearities, symmetry-breaking, mode switching, a large number of meta-stable states, complex equilibrium paths, etc.

One of the first contributions to the study of this particular problem was made by Cao et al. [12]. They performed experiments on microscopic spheres subjected to temperature loading and related numerical simulations in Abaqus [14]. Both approaches showed that spherical systems prefer hexagonal dimple patterns at low over-stress and the labyrinthine (herringbone-like) patterns at high over-stress. The results were confirmed by micro-scale experiments by Breid and Crosby [15] and Yin et al. [16] as well as macro-scale experiments by Terwagne et al. [5] and Brojan et al. [17]. Li et at. [18] used 3D finite elements and a numerical procedure based on the incremental deformation theory involving spherical harmonics on a neo-Hookean hyperelastic bi-layer sphere deformed by volumetric shrinking. A good

---

* Corresponding author.
  E-mail address: miha.brojan@fs.uni-lj.si (M. Brojan).

agreement between the two methods was obtained on the dependence of the critical shrinking factor and the mode number. In addition, their numerical finite element simulations and experiments showed that the sphere first buckles into a dimple pattern, which gradually evolves into a labyrinthine pattern through subsequent bifurcations. The results were confirmed in a study by Stoop et al. [19]. They implemented a model order reduction of the displacement field of the shell by keeping only radial displacements and derived a generalized fourth order Swift-Hohenberg equation. It was solved using a finite-element scheme based on subdivision surface basis functions [20,21] and dynamic relaxation. Furthermore, Veldin et al. [22] used a similar approach to reduce the Kirchhoff–Love shell model and developed a corresponding discrete-Kirchhoff quadrilateral finite element. Together with a path-following algorithm [23], this method proved to be computationally efficient in predicting the characteristic wrinkling pattern at initial post-buckling. Another efficient computational model for predicting the formation of surface wrinkling in shell/substrate composites was recently published by Lavrenčič et al. [24]. Implicit dynamics with energy-decaying time stepping scheme that numerically dissipate in the high frequency range was applied to capture the initial buckling patterns and the transitions between the wrinkling modes in the far post-buckling regime. The geometrically exact, rotationless, nonlinear shell finite element [25] was used to model the shell. The method was tested on axially compressed cylindrical shell-core composites as in the work of Xu and Potier-Ferry [26]. In their study Xu and Potier-Ferry investigated the formation and evolution of the wrinkling pattern. They used a static approach with a geometrically nonlinear 7-parameter shell model (see e.g. [27,28]) for the outer layer, approximated with an 8-node 3D-shell element with reduced integration, soft core discretization with an 8-node linear 3D-solid finite element with reduced integration and an advanced path-following technique [29]. To characterize the forming surface pattern, they defined a dimensionless parameter $C_s = E_s/E_f (R/t)^{3/2}$, where E_s/E_f is the Young modulus ratio of the substrate and the shell and R/t is the radius of the shell's curvature normalized with its thickness. In their recent work, Xu et al. [30] confirmed the validity of this parameter also for spherical geometry.

In this paper we compare four computational models for predicting the wrinkling pattern at the onset of instabilities of thin shell-soft core composites. For two models considered, we apply model order reduction (see [19,22]) by assuming that the tangential displacements are much smaller than the normal ones and can thus be neglected. The first is our recent model from Veldin et al. [22], which is a reduced-order discrete-Kirchhoff–Love formulation and the second is a reduced-order geometrically exact inextensible director shell formulation that enforces Kirchhoff kinematic constraint in a penalty manner by large transverse shear moduli (as proposed e.g. in [31]). Moreover, the latter model is extended in the third model to a framework of nonlinear dynamics by applying an energy-decaying time-stepping algorithm, which exhibits an excellent performance for numerically stiff problems, typical for shells. The fourth model is a dynamic, geometrically exact large rotation formulation [32,33] with energy-decaying integrator [34]. In all cases, the Winkler-type foundation is used to account for the contribution of the shell's substrate, the same as in e.g. [19,22,24,30]. A comparison with other models from the literature on shells with five different values of the dimensionless parameter C_s demonstrates that the four models can solve this highly nonlinear problem. Furthermore, the selection of the models allows the comparison of (*i*) order reduction versus full kinematics, (*ii*) statics versus dynamics and (*iii*) discrete-Kirchhoff versus quasi-Kirchhoff assumptions for the problem of pressurized shell-core systems.

Further details on all the computational models compared in this paper are given in Section 2. In Section 3 we present the spherical shell-core systems and wrinkling patterns together with their evolution diagrams obtained by all four models and discuss the results. The conclusions are drawn in Section 4.

2. Computational models

In this section, we briefly describe the computational models for shells on elastic foundation that will be used below for numerical simulations of wrinkling of shell-core systems.

2.1. Kirchhoff–Love shell model

The initial shell configuration for the Kirchhoff–Love shell model is described as

$$\boldsymbol{x}(\theta^1, \theta^2, \theta^3) = {}_0\boldsymbol{x}(\theta^1, \theta^2) + \theta^3 \boldsymbol{a}_3(\theta^1, \theta^2), \quad {}_0\boldsymbol{x}_{,\alpha} \cdot \boldsymbol{a}_3 = 0, \tag{1}$$

where θ^1 and θ^2 are the convective curvilinear coordinates of the shell mid-surface, $\theta^3 \in [-h/2, h/2]$ is the through-the-thickness convective coordinate (h is the thickness), ${}_0\boldsymbol{x}$ is a vector field indicating the position of the mid-surface in the space, $\boldsymbol{a}_3$ is a unit mid-surface normal vector field, and $(.)_{,\alpha} = \partial(.)/\partial\theta^\alpha$. In the following, the symbol ˜ will denote the objects of the deformed configuration. Because of the Kirchhoff's kinematic constraint, the latter is described simply by adding ˜ to the objects describing vector fields in (1). The Green–Lagrange membrane and bending strains are

$$\epsilon_{\alpha\beta} = \frac{1}{2}(\boldsymbol{u}_{,\alpha} \cdot \boldsymbol{u}_{,\beta} + \boldsymbol{u}_{,\alpha} \cdot \boldsymbol{a}_\beta + \boldsymbol{a}_\alpha \cdot \boldsymbol{u}_{,\beta}), \tag{2}$$

$$\kappa_{\alpha\beta} = -(\tilde{\boldsymbol{a}}_3 \cdot (\boldsymbol{a}_{\alpha,\beta} + \boldsymbol{u}_{,\alpha\beta}) - b_{\alpha\beta}), \tag{3}$$

respectively, where $\boldsymbol{u} = {}_0\tilde{\boldsymbol{x}} - {}_0\boldsymbol{x}$ is the displacement vector, $\boldsymbol{a}_\alpha = {}_0\boldsymbol{x}_{,\alpha}$ is the covariant base vector at the initial configuration, and $b_{\alpha\beta} = -\boldsymbol{a}_\alpha \cdot \boldsymbol{a}_{3,\beta}$ is the initial curvature at the considered mid-surface point. Let us use the Voigt's notation for the strains and energy conjugated second Piola–Kirchhoff membrane forces and bending moments as

$$\boldsymbol{\epsilon} = [\epsilon_{11}, \epsilon_{22}, 2\epsilon_{12}]^T, \qquad \boldsymbol{\kappa} = [\kappa_{11}, \kappa_{22}, 2\kappa_{12}]^T, \tag{4}$$

$$\boldsymbol{n} = [n^{11}, n^{22}, n^{12}]^T, \qquad \boldsymbol{m} = [m^{11}, m^{22}, m^{12}]^T. \tag{5}$$

The relations between the vectors in Eqs. (4) and (5), which take into account the plane stress condition, are $\boldsymbol{n} = \boldsymbol{H}_m \boldsymbol{\epsilon}$ and $\boldsymbol{m} = \boldsymbol{H}_b \boldsymbol{\kappa}$, where $\boldsymbol{H}_m = \frac{Eh}{1-\nu^2}\boldsymbol{H}$, $\boldsymbol{H}_b = \frac{Eh^3}{12(1-\nu^2)}\boldsymbol{H}$, and (see e.g. [35])

$$\boldsymbol{H} = \begin{bmatrix} a^{11}a^{11} & \nu a^{11}a^{22} + (1-\nu)a^{12}a^{12} & a^{11}a^{12} \\ \nu a^{11}a^{22} + (1-\nu)a^{12}a^{12} & a^{22}a^{22} & a^{22}a^{12} \\ a^{11}a^{12} & a^{22}a^{12} & \frac{1-\nu}{2}a^{11}a^{22} + \frac{1+\nu}{2}a^{12}a^{12} \end{bmatrix}. \tag{6}$$

Here, E is elastic modulus and ν is Poisson's ratio. The components of the contravariant mid-surface metric tensor $a^{\alpha\beta} = \boldsymbol{a}^\alpha \cdot \boldsymbol{a}^\beta$ in Eq. (6) follow from the relation $\boldsymbol{a}_\alpha \cdot \boldsymbol{a}^\beta = \delta_\alpha^\beta$, where δ_α^β is the Kronecker delta symbol. With this notation at hand, we can write the potential energy for the Kirchhoff–Love shell on elastic foundation as

$$\Pi(\boldsymbol{u}) = \int_{\mathcal{M}} \frac{1}{2}(\boldsymbol{\epsilon} \cdot \boldsymbol{H}_m \boldsymbol{\epsilon} + \boldsymbol{\kappa} \cdot \boldsymbol{H}_b \boldsymbol{\kappa}) \, dA + \int_{\mathcal{M}} \frac{1}{2}K_s (u_3)^2 \, dA - \int_{\mathcal{M}} u_3 \, p \, dA, \tag{7}$$

where p is the surface pressure acting in the direction of $\boldsymbol{a}_3$, K_s is the spring stiffness representing the substrate reaction in the opposite direction of the pressure action, $u_3 = \boldsymbol{u} \cdot \boldsymbol{a}_3$, and $\mathcal{M}$ is the shell's mid-surface. The minimum of the potential energy can be written as

$$\delta\Pi(\boldsymbol{u}, \delta\boldsymbol{u}) = \int_{\mathcal{M}} (\delta\boldsymbol{\epsilon} \cdot \boldsymbol{H}_m \boldsymbol{\epsilon} + \delta\boldsymbol{\kappa} \cdot \boldsymbol{H}_b \boldsymbol{\kappa}) \, dA + \int_{\mathcal{M}} \delta u_3 \, K_s \, u_3 \, dA$$
$$- \int_{\mathcal{M}} \delta u_3 \, p \, dA = 0, \tag{8}$$

where δ denotes variation and $\delta\boldsymbol{\epsilon} = [\delta\epsilon_{11}, \delta\epsilon_{22}, 2\delta\epsilon_{12}]^T$ and $\delta\boldsymbol{\kappa} = [\delta\kappa_{11}, \delta\kappa_{22}, 2\delta\kappa_{12}]^T$ are variations of strains. Eq. (8) corresponds to the weak form of the considered mechanical problem.

A reduced-order Kirchhoff–Love shell theory, which is the basis for the first computational model considered in this work, is obtained by neglecting the tangential displacements and thus assuming

$$\boldsymbol{u} = u_3 \boldsymbol{a}_3. \tag{9}$$

This considerably simplifies the equations of the theory presented above, as shown in [19] and [22].

A reduced-order, discrete-Kirchhoff finite element with four nodes, which will be used in the section with numerical examples, was derived and presented in detail in [22]. In the following it is referred to as DKQ-3 (as a discrete-Kirchhoff quadrilateral with 3 degrees of freedom per node). Because of the applied linked interpolation [36], DKQ-3 provides a higher-order interpolation for membrane forces and bending moments.

2.2. Geometrically exact shell models

The geometrically exact shell model with Reissner–Mindlin kinematics describes the initial configuration as in Eq. (1). However, the deformed shell configuration is given as

$$\tilde{x}(\theta^1, \theta^2, \theta^3) = {}_0\tilde{x}(\theta^1, \theta^2) + \theta^3 \tilde{a}_3(\theta^1, \theta^2), \quad {}_0\tilde{x}_{,\alpha} \cdot \tilde{a}_3 \neq 0 \,(\text{in general}). \quad (10)$$

The deformed shell-director vector $\tilde{a}_3$ is obtained by a rigid rotation of the initial normal vector a_3 as $\tilde{a}_3 = \Lambda(\vartheta_1, \vartheta_2)a_3$, where Λ is a rotation matrix parametrized by two suitable rotational parameters ϑ_1 and ϑ_2 (zero drilling rotation is adopted). For a discussion on different parametrizations of large rotations for shells we refer to [37]. The Green–Lagrange membrane strains are as in Eq. (2), and the bending and the transverse shear strains are computed as

$$\kappa_{\alpha\beta} = \frac{1}{2}(\tilde{a}_\alpha \cdot \tilde{a}_{3,\beta} + \tilde{a}_\beta \cdot \tilde{a}_{3,\alpha} - a_\alpha \cdot a_{3,\beta} - a_\beta \cdot a_{3,\alpha}), \quad (11)$$

$$\gamma_{\alpha 3} = (\tilde{a}_\alpha \cdot \tilde{a}_3 - a_\alpha \cdot a_3). \quad (12)$$

The relation between the membrane strains ϵ and the bending strains (11) collected in κ, and the second Piola–Kirchhoff membrane forces n and bending moments m, see Eqs. (4) and (5), is still valid through relations $n = H_m \epsilon$ and $m = H_b \kappa$. Additionally, the transverse shear strains and forces appear as

$$\gamma = \begin{bmatrix} \gamma_{13}, \gamma_{23} \end{bmatrix}^T, \qquad q = \begin{bmatrix} q_{13}, q_{23} \end{bmatrix}^T, \quad (13)$$

which are related as $q = G H_s \gamma$, where

$$H_s = c\,h \begin{bmatrix} a^{11} & a^{12} \\ a^{12} & a^{22} \end{bmatrix}. \quad (14)$$

Here, G denotes the transverse shear modulus and c is the shear correction factor (usually set to 5/6 for isotropic shells). The potential energy for this shear deformable formulation has the following form

$$\Pi(u, \vartheta) = \int_{\mathcal{M}} \frac{1}{2}(\epsilon \cdot H_m \epsilon + \kappa \cdot H_b \kappa + G\gamma \cdot H_s \gamma)\,dA + \int_{\mathcal{M}} \frac{1}{2} K_s (u_3)^2 \,dA$$
$$- \int_{\mathcal{M}} u_3\, p\, dA, \quad (15)$$

where $\vartheta = [\vartheta_1, \vartheta_2]^T$. The minimum of the potential energy (15) can be written as

$$\delta\Pi(u, \vartheta, \delta u, \delta\vartheta) =$$
$$\int_{\mathcal{M}} (\delta\epsilon \cdot H_m \epsilon + \delta\kappa \cdot H_b \kappa + G\,\delta\gamma \cdot H_s \gamma)\,dA + \int_{\mathcal{M}} \delta u_3 K_s u_3\, dA$$
$$- \int_{\mathcal{M}} \delta u_3\, p\, dA = 0, \quad (16)$$

where $\delta\gamma = [\delta\gamma_{13}, \delta\gamma_{23}]^T$ is the variation of the transverse shear strains. The variation of the shell director relates to the variation of the rotational parameters as $\delta\tilde{a}_3 = A\delta\vartheta$, with A depending on the chosen parametrization of the finite rotations, see e.g. [37] for details.

In the dynamic setting, the total energy of the shell is a sum of kinetic and potential energy

$$E(u, \vartheta) = \frac{1}{2} \int_{\mathcal{M}} (A_{\rho_0}\dot{u} \cdot \dot{u} + I_{\rho_0}\dot{\tilde{a}}_3 \cdot \dot{\tilde{a}}_3)\,dA + \Pi(u, \vartheta), \quad (17)$$

where $A_{\rho_0} = \rho_0 h$ and $I_{\rho_0} = \rho_0 h^3/12$ are mass inertia terms, ρ_0 is the initial mass density and the dot denotes the derivative with respect

to time t. The principle of least action can be used to obtain the corresponding variational equation of the above functional, which can be written as equivalent d'Alembert equations (see e.g. [38]) in terms of variation of displacements δu and rotations $\delta\vartheta$

$$G_{dyn}(u, \vartheta, \delta u, \delta\vartheta) = \int_{\mathcal{M}} (A_{\rho_0}\ddot{u} \cdot \delta u + I_{\rho_0}\ddot{\tilde{a}}_3 \cdot \delta\tilde{a}_3)\,dA + \delta\Pi(u, \vartheta, \delta u, \delta\vartheta) = 0.$$
$$(18)$$

Eq. (18) requires spatial (i.e. finite element) discretization as well as the time-stepping algorithm for the integration in time.

In the section with numerical examples, we use a dynamic shell formulation based on the above equations and denote it as RM-5-Dy (as Reissner–Mindlin element with 5 degrees of freedom per node for dynamics). This is the second computational model considered in this work. As for the spatial discretization, RM-5-Dy is the standard four-node shell finite element with bi-linear interpolations for the mid-surface and shell director field. Because it uses the assumed natural strain concept of Dvorkin and Bathe [39] for the transverse shear strains, it is sometimes referred to as MITC4 element, see e.g. [40]. We refer to e.g. [41] and [37] for description of the implementation of these interpolations, and for the singularity-free description of the motion of the shell director, respectively. As for the time discretization, we apply the energy-decaying time-stepping algorithm [34,42] that possesses the following property

$$(K_{n+1} - K_n) + (\Pi_{n+1} - \Pi_n) + \mathcal{D} = 0 \quad (19)$$

for free motion, which guarantees unconditional stability for nonlinear dynamics. Here, K is kinetic energy, Π is potential energy, $\mathcal{D} \geq 0$ is dissipation of the total energy within the time interval, and subscripts n and $n + 1$ denote the values at subsequent time points $t_{n+1} > t_n$. The range of dissipation depends on the user-defined parameters α and β, which control the dissipation of kinetic and potential energy. The dissipative properties of the applied energy-decaying scheme with respect to some more common numerically dissipative schemes are presented in [24,42,43]. It is worth noting that the numerical dissipation is essential in the dynamics of shells that is represented by numerically stiff equations. The latter is because of the large difference between the flexible bending/wrinkling and the much stiffer membrane deformation modes. It is desirable that high frequencies are dissipated, because they are an artifact of spatial discretization, and that the fundamental frequencies are not affected by numerical dissipation. The applied energy-decaying scheme has such a property.

In the section with numerical examples, we also use a dynamic finite element formulation called QKQ-3-Dy (as quasi-Kirchhoff quadrilateral element with 3 degrees of freedom per node for dynamics), which is based on a reduced-order version of the above described shell theory. This is the third computational model considered in this work. It applies Eq. (9) that neglects the tangential displacements and considerably simplifies the kinematics of the geometrically exact shell model. Since this assumption does not fit well with the shear-deformable model, we further apply a quasi-Kirchhoff–Love simplification by using a large value for G (of the order $\sim 10^5 E$) in Eq. (14), which plays the role of the penalty number in the computations and allows only negligible transverse shear strains. The spatial and temporal discretizations of QKQ-3-Dy are the same as for RM-5-Dy. The difference between QKQ-3-Dy and RM-5-Dy is that the former formulation uses kinematic constraint (9) and mimics the Kirchhoff–Love solution (because of large value for shear modulus G), whereas the latter does not use any simplifications or modifications.

In the section with numerical examples, the static version of QKQ-3-Dy, denoted as QKQ-3 is also used. This is the fourth and the last computational model considered in this work. The QKQ-3 has similarities with DKQ-3: both are based on reduced kinematics and both tend to generate a Kirchhoff–Love solution for the problem of shell on an elastic foundation. The first major difference between the formulations is the

Table 1
Properties of applied computational models.

FE model	Neglection of tangential displacements	Reissner-Mindlin kinematics	Kirchhoff-Love kinematics	Large shear modulus (penalty number)	Statics	Dynamics
DKQ-3	✓	–	✓	–	✓	–
QKQ-3	✓	✓	–	✓	✓	–
QKQ-3-Dy	✓	✓	–	✓	–	✓
RM-5-Dy	–	✓	–	–	–	✓

approximation order of the membrane forces and bending moments, which is much higher for DKQ-3 due to the linked interpolation that can be applied when the starting point is zero-shear Kirchhoff–Love shell model. The second major difference is that the DKQ-3 allows the use of derivatives of normal displacement as rotational degrees of freedom, whereas QKQ-3 has to apply parametrization of finite rotations. Nevertheless, it is expected that DKQ-3 and QKQ-3 will provide similar numerical solutions for finer meshes.

3. Results and discussion

The finite element codes of the considered shell formulations were generated using the Mathematica's add on AceGen [44], which enables an automatic differentiation of large expressions and algorithms. The codes were further included into the nonlinear finite element computer code AceFEM [45].

3.1. Summary of computational models

The shell-core systems specified below were simulated by four finite element computational models briefly presented in Section 2 and summarized in Table 1. We note that all derived finite elements are quadrilaterals with four nodes. As mentioned above, these computational models are named as follows:

- QKQ-3 and QKQ-3-Dy denote the static and dynamic formulations with reduced-order, quasi-Kirchhoff kinematics that is imposed by large transverse shear modulus. The QKQ-3-Dy uses energy-decaying time-stepping scheme.
- DKQ-3 denotes the static formulation with reduced-order, discrete-Kirchhoff kinematics that is described in detail in [22].
- RM-5-Dy denotes the dynamic, large rotation, geometrically exact, shell formulation (its rotation-free version, see [25], was already applied for cylinders on substrates in [24]). The RM-5-Dy uses energy-decaying time-stepping scheme.

Static analyses with DKQ-3 and QKQ-3 were performed using the path-following method presented in [23]. The identification of critical points and solution branches of the equilibrium paths were not tracked. For QKQ-3 and QKQ-3-Dy a large artificial transverse shear modulus of order $G = 10^5 E$ was prescribed, which restricted the development of the transverse shear strains and numerically enforced kinematics that resembles the Kirchhoff–Love's.

Dynamic analyses with RM-5-Dy and QKQ-3-Dy were performed by the energy-decaying time stepping scheme presented in [42] and [34] (for comparison of the applied time integration with more traditional ones, we refer to [43]). The user-defined parameters that control numerical dissipation in the high-frequency range in the kinetic and potential energy were each set to $\alpha = \beta = 0.5$, thus introducing a considerable degree of numerical dissipation into the algorithm. We note that numerical dissipation is favorable because it eliminates adverse effects of spurious higher frequency modes on the numerical solution. High frequencies are an artifact of spatial discretization and do not reflect the high frequencies of the original continuum problem. For accurate representation of short waves in the elastic continuum, an extremely fine mesh is required, and since such meshes are usually not a viable option in structural dynamics, numerical damping of vaguely represented short waves associated with high-frequency modes

is desirable. In the case of surface wrinkling, numerical dissipation effectively eliminates the erroneous high-frequency modes that pollute the wrinkling pattern and allows smoother development of wrinkles throughout the sphere and a smoother continuation of the analysis after the initial wrinkling pattern formation. The adaptive time step algorithm was applied with the largest and smallest allowed time steps of $\Delta t = 0.5$ s and $\Delta t = 5 \cdot 10^{-7}$ s (except for the largest C_s used, where longer times steps were allowed).

3.2. Properties of spherical shell-core systems

In order to compare and evaluate the proposed computational models, we selected five specific examples of the spherical shell-core system with different material and geometric properties:

- shell-core 1: $E_f = 3000.0$ MPa, $E_s = 3.0$ MPa, $R = 20.0$ mm, $h = 0.35$ mm, $v_f = 0.3$, $v_s = 0.49$, $K_s = 0.8529$ N/mm^3,
- shell-core 2: $E_f = 250$ MPa, $E_s = 2.5$ MPa, $R = 20.0$ mm, $h = 0.4$ mm, $v_f = 0.3$, $v_s = 0.49$, $K_s = 1.3527$ N/mm^3,
- shell-core 3: $E_f = 2.1$ MPa, $E_s = 0.23$ MPa, $R = 20.0$ mm, $h = 0.6$ mm, $v_f = 0.49$, $v_s = 0.49$, $K_s = 0.1738$ N/mm^3,
- shell-core 4: $E_f = 2.1$ MPa, $E_s = 0.23$ MPa, $R = 20.0$ mm, $h = 0.2$ mm, $v_f = 0.49$, $v_s = 0.49$, $K_s = 0.5223$ N/mm^3,
- shell-core 5: $E_f = 25.0$ MPa, $E_s = 3.0$ MPa, $R = 20.0$ mm, $h = 0.05$ mm, $v_f = 0.3$, $v_s = 0.49$, $K_s = 29.8386$ N/mm^3.

Here, E_f, v_f and E_s, v_s denote the Young's modulus and the Poisson's ratio of the shell (i.e. film) and the substrate, respectively, R and h are the radius and the thickness of the shell and

$$K_s = \frac{\bar{E}_s}{mR} \frac{2(1 - v_s)^2 (m^2 - 1)}{3 - 4v_s} \tag{20}$$

is the (Winkler's) foundation constant, as derived in [46], where $\bar{E}_s = E_s/(1 - v_s^2)$, $m = 2\pi R/\lambda$ and $\lambda = 2\pi h(\bar{E}_f/(3\bar{E}_s^*))^{1/3}$, $\bar{E}_f = E_f/(1 - v_f^2)$, $\bar{E}_s^* = 4\bar{E}_s(1 - v_s)^2/(3 - 4v_s)$. The substrate was modeled as a Winkler's foundation (see also [19,22,24,30] for such approach). The values of the characteristic dimensionless parameter, which is defined as $C_s = E_s/E_f(R/h)^{3/2}$ (see [30]), are thus $(C_s) = (0.43, 3.5, 21.1, 109.5, 960)$ for the five systems. The pressure p that is acting on the outer surface of the shell was considered as conservative loading. For dynamic simulations, the loading rate was 10 kPa/s (except for $C_s = 960$, where a slow loading rate 1 kPa/s was used). The initial mass density was assumed to be $\rho_0 = 0.965$ g/cm^3, which corresponds to a mass density of polydimethylsiloxane [47], a material commonly used in experiments on shell-core systems.

No displacement/rotation boundary conditions were applied in the computations. They are not required for dynamics, where the algorithmically consistent tangent matrix is always positive definite. They are also not needed for static analyses of curved surfaces with reduced-order formulations, see [22]. In the reduced-order formulations, the tangential components of the displacements are zero, which already fixes the system in space. Thus, the rigid-body motions of a curved shell element with reduced displacements are not possible, and additional displacements/rotations boundary conditions are redundant, because the consistent tangent matrix will be always positive definite also in statics.
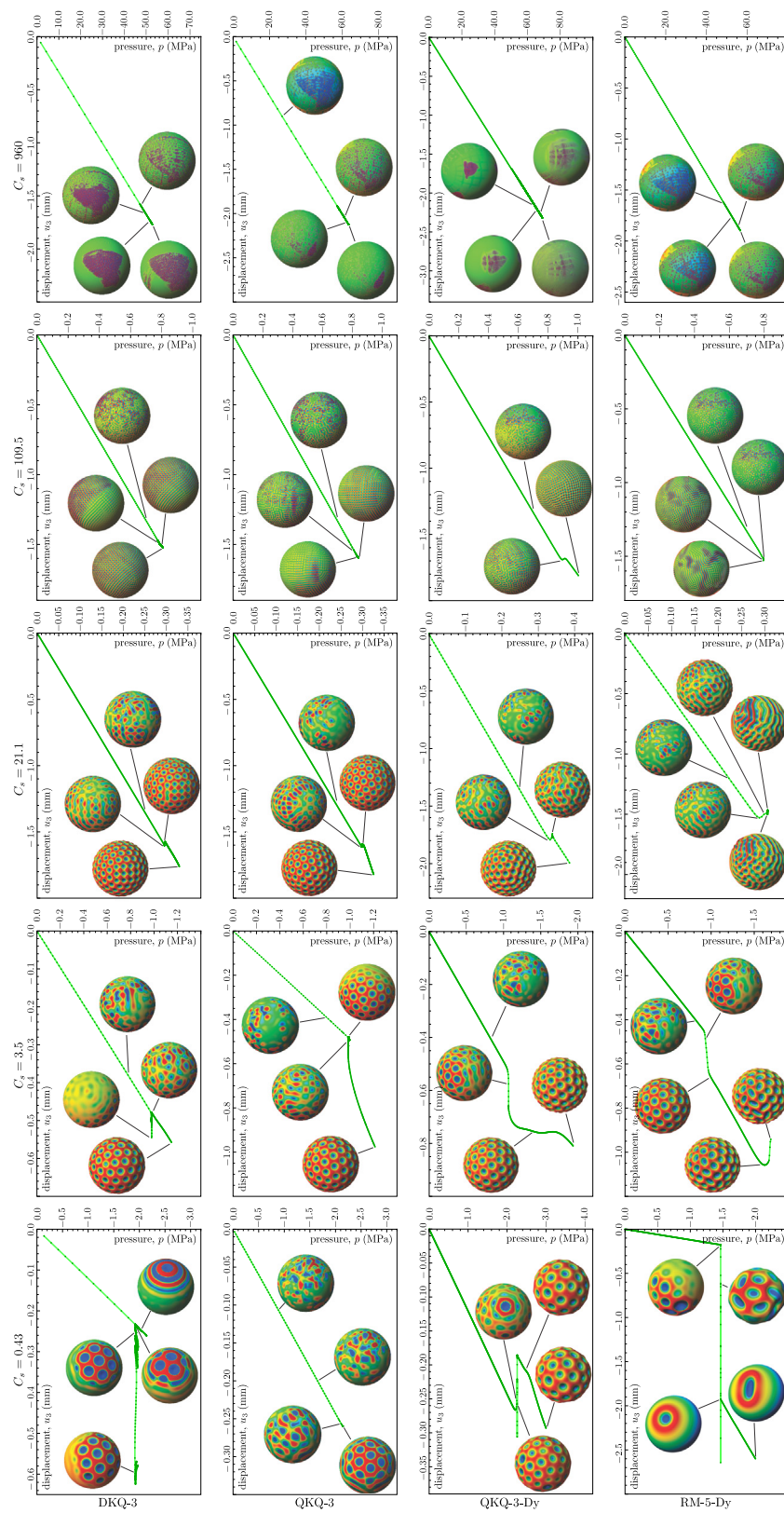
Fig. 1. Pattern evolution and load–displacement paths (p-u_3) for all five shell-core composites and all four computational models.

We used highly non-structured meshes with (n_{el}) = (89 855, 52 431, 89 855, 148 512, 788 534) elements, which corresponds to the characteristic length of the quadrilateral element (l_{avg}) = ($R/83.3$, $R/62.5$, $R/83.3$, $R/125$, $R/250$) for each C_s. The number of elements was selected based on the convergence analysis performed in [22]. During the analysis we monitored the pressure level versus normal displacement of a particular node of the mesh. For each C_s the monitored node remained the same.
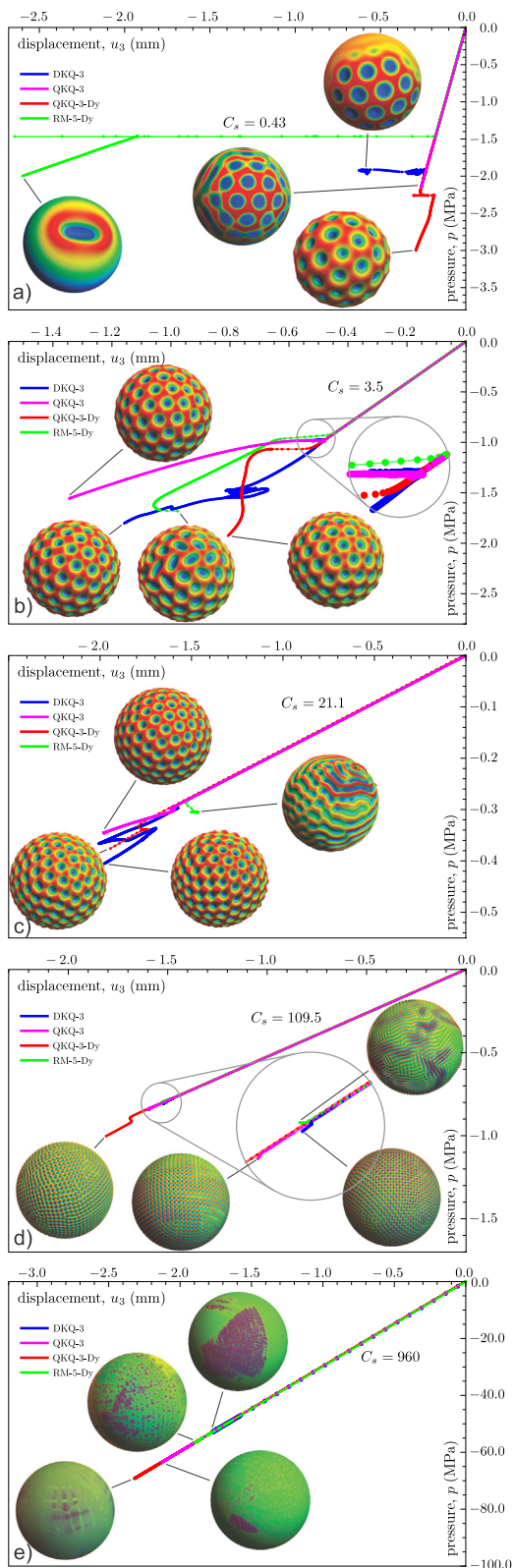
Fig. 2. Comparison of load–displacement paths and end-of-simulation patterns for all five shell-core composites and all four computational models.

3.3. Results of analyses

Fig. 1 summarizes the results of our simulations. It shows a grid of twenty panels, consisting of five columns and four rows. A column

corresponds to a shell-core spherical system with a particular value of C_s and a row corresponds to the applied computational model. The load–displacement diagrams (pressure p versus displacement u_3 of a monitored node of the mesh specified for each C_s) are recorded and snapshots of displacement fields at different pressure levels are taken to show the evolution of the wrinkling pattern.

In all cases, the panels show the transition from an initially uniform spherical deformation (smooth surface) to a deformation pattern with dimples, which eventually evolve into a labyrinthine pattern for one of the computational models. In the first case ($C_s = 0.43$), the DKQ-3 and QKQ-3 models predict that only a part of the sphere is covered by the dimple pattern (around the opposite poles) with a relatively large wavelength (compared to other C_s values) and the rest of the sphere remains smooth, while QKQ-3-Dy predicts a complete coverage by the dimples. Interestingly, at the onset of wrinkling, DKQ-3 and QKQ-3-Dy predict a dominant dimple (more pronounced than the adjacent) at the opposite poles of the sphere around which a small region of a fairly homogenous dimple pattern (mentioned above) is gradually developed as the pressure load is increased. On the other hand, the opposite can be observed in the case of RM-5-Dy. At the onset of wrinkling, this computational model first predicts a small region of dimples (at the two poles), which evolve into an isolated dimple at both poles. Such an isolated dimple mode was also predicted in [48] and [30]. In other cases of the C_s parameter, all computational models predict a fully covered sphere with dimple pattern at small overstress. In two cases, $C_s = 21.1$ and $C_s = 109.5$, only RM-5-Dy predicts further (secondary) transitions to a deformation pattern with channels (labyrinthine pattern), after the deformation pattern with dimples was first vaguely expressed.

A good agreement is also obtained between our results for $C_s = 3.5$ and those of Xu et al. [30], where $C_s = 2.6$ and $C_s = 4.9$ was used. In all three cases the obtained pattern corresponds to the dimple (buckyball) pattern and the wavelength of our simulation is, as expected, between the two from the literature. Note that in our case we used an external pressure to load the system and the reference results were obtained by thermal shrinking, which shows that the wrinkling mechanism is universal and independent of the external stimulus, as mentioned in the introduction. A similar agreement between our results and the results from [30] is obtained in the case of $C_s = 21.1$ (both studies used this value) for the wavelength, but only RM-5-Dy can provide the (dimple-labyrinthine) hybrid pattern. Note that QKQ-3-Dy also showed this pattern before the reverse transformation back to dimples. In the case of $C_s = 109.5$ we obtain on the one hand small-wavelengths dimple patterns, locally arranged in checkerboard mode (which is not an energy minimum mode on a sphere, see e.g. Stoop [19]) for DKQ-3, QKQ-3 and QKQ-3-Dy, and on the other hand small-wavelength labyrinthine pattern in the case of Rm-5-Dy. For the largest C_s, $C_s = 960$, we obtain regions with channel-like wrinkling pattern using DKQ-3 and QKQ-3, a fully covered surface with channel-like pattern in the case of QKQ-3-Dy and not fully developed wrinkling pattern for RM-5-Dy. Ref. [30] reports only the checkerboard dimple mode with smaller wavelength, as even larger value of C_s, $C_s = 1018$, was used. Note also that Xu et al. [30] considered in their numerical model an one-eighth symmetry of the system via symmetrical boundary conditions.

Fig. 1 also shows that as C_s increases, the number of dimples increases (and the characteristic wavelength decreases). Also, the simulations become more difficult to run, because the number of meta-stable states increases rapidly (see Ref. [49] for more details). This is illustrated by the fact that the analyses tend to fail earlier with increasing C_s after the initial formation of the wrinkling pattern.

Fig. 2(a)–(e) show the comparisons of the load–displacement curve and the final wrinkling patterns for each C_s. A complete agreement between the load–displacement (p-u_3) curves is obtained before buckling and, in most cases, a fairly good match between the predictions of buckling pressure at the onset of wrinkling. The critical pressures are approximately: between $p \doteq -1.5$ MPa and $p \doteq -2.2$ MPa for $C_s = 0.43$
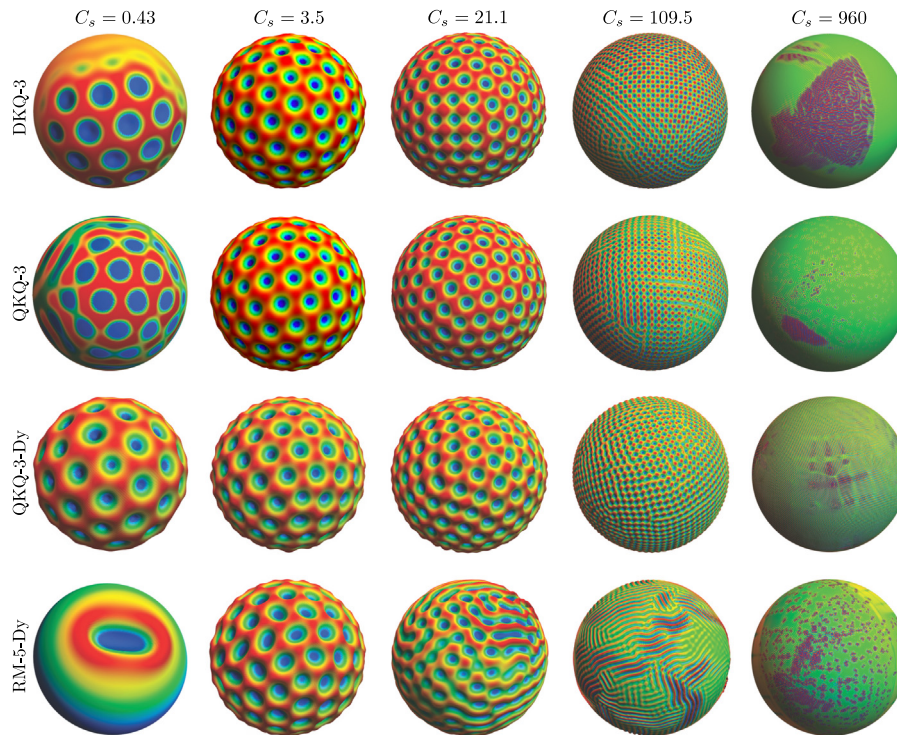
Fig. 3. End-of-simulation patterns for all five shell-core composites and all four computational models.

(see Fig. 2a), $p \doteq -1$ MPa for $C_s = 3.5$ (see Fig. 2b), $p \doteq -0.3$ MPa for $C_s = 21.1$ (see Fig. 2c), $p \doteq -0.8$ MPa for $C_s = 109.5$ (see Fig. 2d) and $p \doteq -50$ MPa for $C_s = 960$ (see Figs. 2(e) and 1). However, further post-buckling paths (in general) do not match. This is because the wrinkling pattern predicted by a particular formulation is slightly different from the wrinkling pattern predicted by another formulation. In other words, the dimples do not appear at the same locations in the mesh, although the patterns (at least for DKQ-3, QKQ-3 and QKQ-3-Dy) are practically the same for a given C_s. During the analysis, the pattern starts to move over the surface, so the monitored node is not always at the same position with respect to the pattern. Its position can change between the dimple, the peak or somewhere in between, which is indicated by a more "wavy" load–displacement curve when zoomed in.

For $C_s = 0.43$ (see Fig. 2a), the computational models provide quite different predictions for the critical buckling pressure, ranging from $p \doteq -1.5$ MPa and $p \doteq -2.2$ MPa (the critical pressure for QKQ-3-Dy is the highest, followed by QKQ-3, DKQ-3 and the lowest buckling pressure is predicted by RM-5-Dy). Similarly, the obtained patterns differ, as the isolated dimple mode is predicted by RM-5-Dy, the partially covered surface by DKQ-3 and QKQ-3 and the completely dimple covered surface by QKQ-3-Dy, as already mentioned above. For $C_s = 3.5$ (see Fig. 2b), all four computational models give similar results in terms of number of dimples and critical pressure. We find that the dimples begin to form on one side of the sphere and propagate across the surface. When the pattern is fully developed, it begins to move slowly across the mesh. This is especially noticeable in DKQ-3, where around -1.5 MPa the pattern is moving substantially, making an intertwined load–displacement curve. It can also be observed that RM-5-Dy starts to stretch the dimples towards the end of the analysis. For $C_s = 21.1$ (see Fig. 2c), RM-5-Dy computes a different end deformation shape than other formulations – it predicts the labyrinthine pattern while other formulations predict dimples. The critical pressure of QKQ-3-Dy is higher than the critical pressures predicted by DKQ-3, QKQ-3 and RM-5-Dy. RM-5-Dy initially predicts a vaguely developed dimple pattern that very quickly transforms into a pattern that is a

mixture of dimples and channels. The average distance between the channels (the wavelength) is in the same range as the wavelengths of the dimple patterns in the other three formulations. For DKQ-3, QKQ-3 and QKQ-3-Dy, the number of dimples is similar. For $C_s = 109.5$ (see Fig. 2d), we again observe that the critical pressure is the highest for QKQ-3-Dy, slightly lower for QKQ-3, and DKQ-3 and RM-5-Dy predict the lowest critical pressure. As for the wrinkling pattern, DKQ-3, QKQ-3 and QKQ-3-Dy all predict similar dimple checkerboard patterns (which are non-optimal), while RM-5-Dy initially predicts a vaguely developed dimple pattern that rapidly transforms into a fully developed labyrinthine pattern. For $C_s = 960$ (see Fig. 2e), we observe that the critical pressure is the highest for QKQ-3 and the others are approximately the same (around -50 MPa).

A more illustrative comparison between the developed patterns is shown in Fig. 3. As before, each column in this figure corresponds to a fixed C_s value of the shell-core system and each row corresponds to the relevant computational model. The u_3 displacement fields were recorded between $p \doteq -1.5$ MPa and $p \doteq -2.2$ MPa for the first column, at approximately $p \doteq -1.5$ MPa for the second column, at $p \doteq -0.35$ MPa for the third column, between $p \doteq -1.0$ MPa and $p \doteq -0.8$ MPa for the fourth column and around $p \doteq -50$ MPa for the fifth column.

We find a relatively good agreement between the patterns in each column, with few exceptions. Namely, (*i*) only RM-5-Dy can compute an isolated dimple mode (see [48] and [30]) for the $C_s = 0.43$, while formulations DKQ-3 and QKQ-3Dy predict a partially dimpled surface (and the rest smooth) and QKQ-3-Dy predicts a fully covered surface), (*ii*) RM-5-Dy predicts for $C_s = 21.1$ and $C_s = 109.5$ a secondary transition from dimple to labyrinthine pattern and (*iii*) for $C_s = 960$ DKQ-3 and QKQ-3 predict localized labyrinthine areas, QKQ-3-Dy predicts a surface fully covered with labyrinthine pattern and RM-5-Dy did not converge in this case. Moreover, we find the following number of dimples $(n) = (2 \times 14, 2 \times (7 - 19), 55, 2 \times 1)$ for $C_s = 0.43$, $(n) = (132, 132, 125, /)$ for $C_s = 3.5$, $(n) = (221, 216, 206, /)$ for $C_s = 21.1$ and around 2000 for the $C_s = 109.5$ case. The number of dimples could not be estimated accurately enough for $C_s = 960$.

Note that the results for each numerical model are given in this order: (DKQ-3, QKQ-3, QKQ-3-Dy, RM-5-Dy) and that the number of dimples for RM-5-Dy (other that for $C_s = 0.43$) were not recorded.

3.4. Performance of computational models

The RM-5-Dy has no kinematic (and other) simplifications, except the one related to the modeling of the substrate by springs, which is, however, common to all four formulations we use. In this sense, the results of RM-5-Dy could be trusted the most. On the other hand, the choice of the time-stepping scheme and the choice of the level of numerical dissipation influence the RM-5-Dy results. As for the time-stepping scheme, we chose the one that decays (or conserves) the energy of the elastic system for autonomous motion, and is in our opinion the most suitable for the problem of surface wrinkling. The controllable energy decaying comes with the price of first-order accuracy, but since very small time steps were used (except in the initial stage of analyses) this should not represent a major problem. We note that numerical dissipation is absolutely necessary for wrinkling simulation with structural dynamics schemes. The high-frequency modes (which are erroneous due to the spatial discretization) need to be damped out to avoid pollution of the results. However, too much dissipation also has undesirable effects on the results, since it also affects the basic, low-frequency modes. How the level of dissipation (controlled by parameters α and β) influences the results can be illustrated for $C_s = 3.5$. In this particular case, the low dissipation caused a non-uniform initiation of dimples (i.e. dimples emerged only on approximately one half of the sphere). This initial pattern was floating and slightly changing continuously, which demanded very small time steps that prevented full pattern formation. Instead, the erroneous high-frequency modes generated some deep dimples with self-contact. For this reason, we chose the approximate minimum level of dissipation that effectively eliminates the high-frequency modes that pollute the results. We should emphasize, however, that the type and the density of the emerging pattern was independent of the chosen level of dissipation.

Furthermore, Fig. 1 shows that for $C_s = 21.1$ and $C_s = 109.5$ the first pattern, which is the dimple-mode, is vaguely represented by the dynamic formulations QKQ-3-Dy and RM-5-Dy, and is immediately replaced by a labyrinth-mode. The labyrinth pattern further evolves for RM-5-Dy, but changes to a dimple pattern for QKQ-3-Dy. This suggests that our dynamic formulations are prone to (almost) skip the first dimple-mode for systems when transition to the labyrinth mode is expected. On the other hand, from the comparison between QKQ-3-Dy and RM-5-Dy for $C_s = 21.1$ and $C_s = 109.5$, it can be concluded that the reduced-order models compute labyrinth as an intermediate pattern and predict dimples as the final pattern even for systems where labyrinth is expected as the final pattern according to RM-5-Dy and [19]. We can conclude that our dynamic formulations mask the first dimple-mode for cases where a transition is expected and that the reduced-order models prefer dimple-mode to the labyrinth-mode for such cases.

The static analysis with RM-5 finite element and our path-following method did not yield any meaningful results due to the failure of the solution method. However, our path-following method was successful in all other cases. We contribute its successful use in the computation of the wrinkling patterns to two factors. The first factor is their application to reduced-order models. Namely, all our static formulations neglect tangential displacements, which reduces small disturbing tangential motions at the onset of the pattern formation and considerably improves the chances of the path-following method to find a solution. The second factor is a careful selection of the parameters governing the arc-length procedure that were changing during the computation.

The purpose of reducing tangential displacements is to reduce the complexity of the problem and provide a solution for static analysis that cannot otherwise be obtained using standard path-following techniques for non-reduced models. However, the comparison of the numerical results shows that the reduction is also useful in the physical sense, since the results of the reduced static models (DKQ-3 and QKQ-3) are comparable to the results of the non-reduced model RM-5-Dy, at least with respect to the first wrinkling pattern. It can be therefore concluded that the models with reduced displacements are suitable for the computations of patterns at the onset of wrinkling. However, is seems that they cannot correctly predict the patterns (at high overstress) when higher order pattern transitions are expected. In this sense, the reduced-order models have similar shortcomings as the linearized buckling models for predicting buckling modes.

In the static analyses we monitored the change in the number of negative pivots of the stiffness matrix, which indicates whether the critical point (either the limit or the bifurcation point) has been passed. In case of $C_s = 3.5$ analysis with DKQ-3, the first negative pivot appears around the formation of the wrinkling pattern. When the analysis continues, 1 negative pivot remains in 8 further steps. After that it switches back to 0 negative pivots. When the analysis continues, the number of negative pivots changes between 1 and 0. The situation is very similar with QKQ-3. In case of $C_s = 21.1$ analysis with DKQ-3 and QKQ-3, the first negative pivot appears after the dimple pattern starts to form. After a few more steps, the number of negative pivots drops back to 0. In case of $C_s = 109.5$, the number of negative pivots for DKQ-3 and QKQ-3 appears after the dimple-channel pattern has already partially formed. With increasing load, the number of negative pivots changes from 0 to 2, but all these limit and bifurcation points are related to the slight rearrangements of the initial pattern and not to the pattern transition.

4. Conclusions

Four computational models were applied to solve the mechanical problem of surface wrinkling of spherical shell-core systems under external pressure. The solution of the problem was searched in the context of both statics and dynamics. For the dynamics and this class of problems, we propose an application of energy-decaying schemes that can dissipate the energy of higher modes and thus control the overall stability of the numerical computations over a long period of time. It was found that the energy-decaying scheme with a high level of dissipation, which can effectively suppress surface movements (associated with spurious high-frequency deformation modes) of the wrinkling pattern after its formation, is efficient for this class of problems.

Based on the above presented computational results, we also propose the use of a simplified approach with reduced-order kinematics, which has proven to be an effective and accurate substitute (at least for small and medium values of the characteristic parameter of the shell-core system C_s) for standard, unmodified finite element procedures. It is important to note that reduced-order computational models can provide a comparable solution (with respect to the wrinkling pattern and critical pressure) compared to an unmodified computational model. This is especially important in view of the fact that standard (static and dynamic) finite element procedures are very likely to fail if they are simply applied to treat this type of problems. Our results show that computational models with reduced-order kinematics provide similar results to unmodified (i.e. standard) formulations for small and medium values of C_s, when the formation of dimple wrinkling pattern is expected. For larger values of C_s, when the formation of (secondary transition to) a labyrinthine wrinkling pattern is likely, the reduced-order models are less accurate.

Finally, we note that in the qualitative prediction of wrinkle patterns we obtain a good agreement between our results and those of Xu et al. [30], where experimental results and numerical results based on one-eight symmetry were reported. In our case, we used external pressure to stimulate the system and the reference results are obtained by thermal shrinkage, which in turn shows that the wrinkle mechanism is universal and independent of the external stimulus.

CRediT authorship contribution statement

Tomo Veldin: Software, Investigation, Formal analysis, Writing - original draft, Visualization. **Marko Lavrenčič:** Software, Investigation, Formal analysis, Writing - original draft. **Boštjan Brank:** Conceptualization, Methodology, Investigation, Supervision, Writing - original draft & review, Funding. **Miha Brojan:** Conceptualization, Investigation, Supervision, Writing - original draft & review, Visualization, Funding.

Declaration of competing interest

The authors declare that they have no known competing financial interests or personal relationships that could have appeared to influence the work reported in this paper.

Acknowledgment

References

[1] J.Y. Chung, J.P. Youngblood, C.M. Stafford, Anisotropic wetting on tunable micro-wrinkled surfaces, Soft Matter 3 (9) (2007) 1163–1169.

[2] E.P. Chan, E.J. Smith, R.C. Hayward, A.J. Crosby, Surface wrinkles for smart adhesion, Adv. Mater. 20 (4) (2008) 711–716.

[3] J.A. Rogers, T. Someya, Y. Huang, Materials and mechanics for stretchable electronics, Science 327 (5973) (2010) 1603–1607.

[4] J.Y. Chung, A.J. Nolte, C.M. Stafford, Surface wrinkling: A versatile platform for measuring thin-film properties, Adv. Mater. 23 (2011) 349–368.

[5] D. Terwagne, M. Brojan, P.M. Reis, Smart morphable surfaces for aerodynamic drag control, Adv. Mater. 26 (38) (2014) 6608–6611.

[6] A.E. Shyer, T. Tallinen, N.L. Nerurkar, et al., Villification: How the gut gets its villi, Science 342 (6155) (2013) 212–2018.

[7] T. Tallinen, J.Y. Chung, F. Rousseau, N. Girard, J. Lefevre, L. Mahadevan, On the growth and form of cortical convolutions, Nat. Phys. 12 (2016) 588–593.

[8] K. Goodwin, S. Mao, T. Guyomar, et al., Smooth muscle differentiation shapes domain branches during mouse lung development, Development 146 (22) (2019) 181172.

[9] C. Fei, S. Mao, J. Yan, et al., Nonuniform growth and surface friction determine bacterial biofilm morphology on soft substrates, Proc. Natl. Acad. Sci. USA 117 (14) (2020) 7622–7632.

[10] J. Yan, C. Fei, S. Mao, et al., Mechanical instability and interfacial energy drive biofilm morphogenesis eLife, 8 (2019) e43920.

[11] Y. Tan, B. Hu, J. Song, et al., Bioinspired multiscale wrinkling patterns on curved substrates: An overview, Nano-Micro Lett. 12 (101) (2020) 1–42.

[12] G. Cao, X. Chen, C. Li, A. Ji, Z. Cao, Self-assembled triangular and labyrinth buckling patterns of thin films on spherical substrates, Phys. Rev. Lett. 100 (3) (2008) 036102(4).

[13] X. Zhang, P.T. Mather, M.J. Bowick, T. Zhang, Non-uniform curvature and anisotropic deformation control wrinkling patterns on tori, Soft Matter 15 (2019) 5204–5210.

[14] Dassault Systemes, Abaqus, url = http://www.3ds.com/productsservices/simulia/products/abaqus/.

[15] D. Breid, A.J. Crosby, Curvature-controlled wrinkle morphologies, Soft Matter 9 (13) (2013) 3624–3630.

[16] J. Yin, X. Han, Y. Cao, C. Lu, Surface wrinkling on polydimethylsiloxane microspheres via wet surface chemical oxidation, Sci. Rep. UK 4 (2014) 5710(8).

[17] M. Brojan, D. Terwagne, R. Lagrange, P.M. Reis, Wrinkling crystallography on spherical surfaces, Proc. Natl. Acad. Sci. USA 112 (1) (2015) 14–19.

[18] B. Li, J. Fei, Y.P. Cao, X.Q. Feng, H. Gao, Surface wrinkling patterns on a core-shell soft sphere, Phys. Rev. Lett. 106 (23) (2011) 234301(4).

[19] N. Stoop, R. Lagrange, D. Terwagne, P.M. Reis, J. Dunkel, Curvature-induced symmetry breaking determines elastic surface patterns, Nature Mater. 14 (2015) 337–342.

[20] F. Cirak, M. Ortiz, P. Schröder, Subdivision surfaces: A new paradigm for thin-shell finite-element analysis, Internat. J. Numer. Methods Engrg. 47 (12) (2000) 2039–2072.

[21] N. Stoop, F.K. Wittel, M. Ben Amar, M.M. Müller, H.J. Herrmann, Self-contact and instabilities in the anisotropic growth of elastic membranes, Phys. Rev. Lett. 105 (2010) 068101.

[22] T. Veldin, B. Brank, M. Brojan, Computational finite element model for surface wrinkling of shells on soft substrates, Commun. Math. Sci. 78 (2019) 104863.

[23] A. Stanić, B. Brank, J. Korelc, On path-following methods for structural failure problems, Comput. Mech. 58 (2016) 281–306.

[24] M. Lavrenčič, B. Brank, M. Brojan, Multiple wrinkling mode transitions in axially compressed cylindrical shell-substrate in dynamics, Thin Wall. Struct. 150 (2020) 106700.

[25] M. Lavrenčič, B. Brank, Simulation of shell buckling by implicit dynamics and numerically dissipative schemes, Thin-Walled Structures 132 (2018) 682–699.

[26] F. Xu, M. Potier-Ferry, On axisymmetric/diamond-like mode transitions in axially compressed core–shell cylinders, J. Mech. Phys. Solids. 94 (2016) 68–87.

[27] B. Brank, J. Korelc, A. Ibrahimbegovic, Nonlinear shell problem formulation accounting for through-the-thickness stretching and its finite element implementation, Comput. Struct. 80 (2002) 699–717.

[28] B. Brank, Nonlinear shell models with seven kinematic parameters, Comput. Methods Appl. Mech. Engrg. 194 (2005) 2336–2362.

[29] N. Damil, M. Potier-Ferry, A new method to compute perturbed bifurcations: Application to the buckling of imperfect elastic structures, Internat. J. Engrg. Sci. 28 (9) (1990) 943–957.

[30] F. Xu, S. Zhao, C. Lu, M. Potier-Ferry, Pattern selection in core–shell spheres, J. Mech. Phys. Solids. 137 (2020) 103892.

[31] R. Eberlein, P. Wriggers, R.L. Taylor, A fully non-linear axisymmetrical quasi-kirchhoff-type shell element for rubber-like materials, Internat. J. Numer. Methods Engrg. 36 (1993) 4027–4043.

[32] B. Brank, L. Briseghella, N. Tonello, F.B. Damjanić, On nonlinear dynamics of shells: Implementation of energy–momentum conserving algorithm for a finite rotation shell model, Internat. J. Numer. Methods Engrg. 42 (1998) 409–442.

[33] B. Brank, An energy conserving non-linear dynamic finite element formulation for flexible composite laminates, Comput. Struct. 80 (2002) 677–689.

[34] B. Brank, J. Korelc, A. Ibrahimbegovic, Dynamics and time-stepping schemes for elastic shells undergoing finite rotations, Comput. Struct. 81 (2003) 1193–1210.

[35] J.C. Simo, D.D. Fox, On a stress resultant geometrically exact shell model. part I: Formulation and optimal parametrization, Comput. Methods Appl. Mech. Engrg. 72 (1989) 267–304.

[36] U. Bohinc, B. Brank, A. Ibrahimbegovic, Discretization error for the discrete kirchoff plate finite element approximation, Comput. Method. Appl. M. 269 (2014) 415–436.

[37] B. Brank, A. Ibrahimbegovic, On the relation between different parametrizations of finite rotations for shells, Eng. Comput. 18 (2001) 950–973.

[38] A. Ibrahimbegovic, Nonlinear Solid Mechanics: Theoretical Formulations and Finite Element Solution Methods, Springer Science & Business Media, 2009.

[39] E.N. Dvorkin, K.J. Bathe, A continuum mechanics based four-node shell element for general nonlinear analysis, Eng. Comput. 1 (1984) 77–88.

[40] M. Lavrenčič, B. Brank, Hybrid-mixed shell quadrilateral that allows for large solution steps and is low-sensitive to mesh distortion, Comput. Mech. 65 (2020) 177–192.

[41] B. Brank, F.B. Damjanić, D. Perić, On implementation of a nonlinear four node shell finite element for thin multilayered elastic shells, Comput. Mech. 16 (1995) 341–359.

[42] I. Romero, F. Armero, Numerical integration of the stiff dynamics of geometrically exact shells: an energy-dissipative momentum conserving scheme, Internat. J. Numer. Methods Engrg. 54 (2002) 1043–1086.

[43] M. Lavrenčič, B. Brank, Comparison of numerically dissipative schemes for structural dynamics: generalized-alpha versus energy-decaying methods, Thin-walled structures (2020) in print.

[44] J. Korelc, P. Wriggers, Automation of Finite Element Methods, Springer Inter-national Publishing, 2016.

[45] J. Korelc, AceFEM, 2020, available at http://symech.fgg.uni-lj.si/.

[46] R. Lagrange, F. Lopez Jimenez, D. Terwagne, M. Brojan, P.M. Reis, From wrinkling to global buckling of a ring on a curved substrate, J. Mech. Phys. Solids. 89 (2016) 77–95.

[47] Polymerdatabase.com:, 2019, URL: https://polymerdatabase.com/polymers/Polydimethylsiloxane.html (Accessed on 2019).

[48] B. Audoly, J.W. Hutchinson, Localization in spherical shell buckling, J. Mech. Phys. Solids. 136 (2020) 103720.

[49] T. Erber, G.M. Hockney, Equilibrium configurations of N equal charges on a sphere, J. Phys. A: Math. Gen. 24 (23) (1991) 1369–1377.